REPORT DOCUMENTATION PAGE

AFRL-SR-BL-TR-01-

0159

1. AGENCY USE ONLY (Leave blank)	2. REPORT DATE 1 March 2001	3. REPORT TYPE AND .... – 30 Nov. 1999 Final Technical Report

4. TITLE AND SUBTITLE Soot Formation in Turbulent Combusting Flows	5. FUNDING NUMBERS PE-61102F PR-2308 SA-BS G-F49620-97-1-0094
6. AUTHOR(S) Robert J. Santoro	

7. PERFORMING ORGANIZATION NAME(S) AND ADDRESS(ES) The Pennsylvania State University 240 Research Building East University Park, PA 16802	8. PERFORMING ORGANIZATION REPORT NUMBER

9. SPONSORING / MONITORING AGENCY NAME(S) AND ADDRESS(ES) AFOSR/NA 801 North Randolph St, Room 732 Arlington, VA 22203-1977	10. SPONSORING / MONITORING AGENCY REPORT NUMBER

11. SUPPLEMENTARY NOTES

AIR FORCE OFFICE OF SCIENTIFIC RESEARCH (AFOSR)

12a. DISTRIBUTION / AVAILABILITY STATEMENT Approved for public release; distribution is unlimited	NOTICE OF TRANSMITTAL DTIC. THIS TECHNICAL REP... 12b. DISTRIBUTION CODE HAS BEEN REVIEWED AND IS APPROVED FOR PUBLIC RELEASE LAW AFR 190-12. DISTRIBUTION IS UNLIMITED.

13. ABSTRACT (Maximum 200 Words)

This study investigated the effects of turbulence on the spatial distribution of the soot particle and OH· fields in turbulent C_2H_4 air/jet diffusion flames. Measurements obtained using planar laser-induced incandescence (LII) for soot volume fraction and laser-induced fluorescence (LIF) for both OH·, and polycyclic aromatic hydrocarbons (PAH) formed the basis for investigating soot formation and destruction processes in these flames. These laser-based techniques were applied to the flame independently as well as simultaneously. Extensive information on the structure of the soot and OH· fields was obtained from two-dimensional imaging experiments. Imaging results for soot, OH· and PAH indicated three distinct soot formation/oxidation regions: a rapid soot growth region, in which OH· and soot particles lie in distinctly different radial locations; a mixing dominated region controlled by large-scale fluid motion; and, finally, a soot oxidation region in which the OH· and soot fields overlap spatially, resulting in the rapid oxidation of soot particles. Detailed quantitative analyses including soot volume fraction, OH· and soot zone thickness variations, and probabilities distributions for soot and OH· were performed. The measurements of soot and OH· zone thickness showed that the soot zone thickness varied nearly linearly in the formation region, while approximately a doubling of thickness of the OH· zone was evident over the studied Reynolds number range (4000-23000). The probability density function results for soot, OH·, and PAH indicated that OH· and PAH are spatially interrelated with respect to soot formation and oxidation processes

14. SUBJECT TERMS soot formation, turbulent flames, particles, flames			15. NUMBER OF PAGES 31
			16. PRICE CODE

17. SECURITY CLASSIFICATION OF REPORT UNCLASSIFIED	18. SECURITY CLASSIFICATION OF THIS PAGE UNCLASSIFIED	19. SECURITY CLASSIFICATION OF ABSTRACT UNCLASSIFIED	20. LIMITATION OF ABSTRACT UL

NSN 7540-01-280-5500

Standard Form 298 (Rev. 2-89)
Prescribed by ANSI Std. Z39-18
298-102

Final Report
on
Soot Formation in Turbulent Combusting Flows

for
AFOSR Contract/Grant F49620-97-1-0094

Prepared by

Robert J. Santoro
Propulsion Engineering Research Center
and
Department of Mechanical and Nuclear Engineering
The Pennsylvania State University
University Park, PA 16802

Submitted to:

Air Force Office of Scientific Research
801 North Randolph Road, Room 732
Arlington, VA 22203-1977

March 2001

20010326 119

EXECUTIVE SUMMARY

This study investigated the effects of turbulence on the spatial distribution of the soot particle and OH· fields in turbulent C_2H_4 air/jet diffusion flames. Measurements obtained using planar laser-induced incandescence (LII) for soot volume fraction and laser-induced fluorescence (LIF) for both OH·, and polycyclic aromatic hydrocarbons (PAH) formed the basis for investigating soot formation and destruction processes in these flames. These laser-based techniques were applied to the flame independently as well as simultaneously. Extensive information on the structure of the soot and OH· fields was obtained from two-dimensional imaging experiments. Imaging results for soot, OH· and PAH indicated three distinct soot formation/oxidation regions: a rapid soot growth region, in which OH· and soot particles lie in distinctly different radial locations; a mixing dominated region controlled by large-scale fluid motion; and, finally, a soot oxidation region in which the OH· and soot fields overlap spatially, resulting in the rapid oxidation of soot particles. Detailed quantitative analyses including soot volume fraction, OH· and soot zone thickness variations, and probabilities distributions for soot and OH· were performed. The measurements of soot and OH· zone thickness showed that the soot zone thickness varied nearly linearly in the formation region, while approximately a doubling of thickness of the OH· zone was evident over the studied Reynolds number range (4000-23000). The probability density function results for soot, OH·, and PAH indicated that OH· and PAH are spatially interrelated with respect to soot formation and oxidation processes.

TABLE OF CONTENTS

1.0 INTRODUCTION

Current interest in high performance, low emissions gas turbine engines by the Air Force underscores the need for research on soot formation processes, since soot formation is directly related to issues involving performance and operability. Although recent research has provided significant advances in terms of understanding the basic mechanism controlling soot formation and destruction, many questions still remain. In particular, an understanding of soot formation under high pressure and turbulent flame conditions is lacking. Since gas turbine combustors characteristically involve such flow, it is necessary to address these conditions if further progress is to be made. The current research project was specifically directed at providing measurements of soot formation and destruction in atmospheric pressure turbulent diffusion flames. Since the variation in density in turbulent flames is quite large in most cases, measuring techniques to determine accurate emissions are of great interest, both for combustion science and industrial applications. Information on soot is critically needed to better understand the elementary combustion process, in order to reduce pollutant formation without compromising combustion efficiency.

Prior studies associated with soot measurements in turbulent flames have sought to identify soot formation mechanisms under various conditions [1-7]. However, most of these experiments were conducted using laser extinction/absorption methods yielding results that may not be applicable to turbulent flames. The two-color pyrometry technique combined with absorption provides a joint measurement of temperature and soot volume fraction enabling researchers to identify the effect of temperature on soot formation [5-7]. Although the compact optical probe used for these measurements has some advantages over traditional optical measurements, a relatively large probe volume is still required to detect sufficient signals, which reduces the spatial resolution. In addition, insertion of the probe into the flame affects the flow field, which introduces additional unknown uncertainties.

Recent work emphasizing the use of planar imaging by laser light scattering has revealed the soot structure associated with the flow field. Although a two-dimensional (2-D) laser light scattering method is a possible candidate to overcome the spatial limitation intrinsic to absorption techniques [8-9], the scattering signal is highly dependent on the particle size and weights larger particle sizes much more heavily. Thus, light scattering measurements cannot provide a true measurement of soot concentrations. Recently, laser-induced incandescence (LII)

has been shown to be capable of providing measurements of soot volume fraction in a variety of combustion environments [5-14]. This technique utilizes a short (~ 10 ns), high intensity laser pulse to heat soot particles, with the subsequently detected particle incandescence serving as a measure of the soot volume fraction. This laser diagnostic technique has been employed to measure soot volume fraction in laminar [13], flickering [14], and turbulent [15] flames, although results are very limited for turbulent diffusion flames. Measurements utilizing point, line, and planar sheets have been reported, which provide spatially- and temporally- resolved information on these soot particle fields. Thus, LII is more applicable for visualizing and quantifying soot structures in turbulent diffusion flames and has been selected for use in the present studies.

The examination of spatial variations of OH· associated with different flame conditions is also very important since soot oxidation is largely due to reactions with OH· under many flame conditions [16]. Hydroxyl radical (OH·) images measured by planar laser-induced fluorescence (PLIF) reveal the flame reaction zone that affects the formation and oxidation processes of the soot particles. Through comparisons of the soot particle and OH· fields under varying flame conditions, information on the evolution of soot formation and oxidation processes can be obtained.

The research work reported here addresses understanding of the spatial relationship between the soot formation process associated with various flame conditions and OH· fields present in turbulent ethylene-air jet flames. The study is concerned specifically with providing measurements of soot formation and destruction mechanisms in atmospheric pressure turbulent diffusion flames. Measurements of the soot volume fraction and relative OH· concentrations have been obtained from atmospheric flames over a Reynolds number range of 4000 to 23000 for ethylene jet flames. These measurements have yielded quantitative information on the quantity of soot formed, the probability density functions for soot volume fraction, and relative OH· and polycyclic aromatic hydrocarbons (PAH) concentrations as functions of flame position and Reynolds number. These results are intended to form the basis for validation of models of flame systems, for example, representative of gas turbine combustors. Such modeling capability is required to develop the insight necessary for advancing design methodology for these complex flame systems in terms of reducing soot in both the combustor and the engine exhaust stream.

2

2.0 EXPERIMENTAL APPROACH

Burner Configuration

The schematic of the burner arrangement used for the experiments is shown in Fig. 1. The center fuel nozzle (2.18 mm I.D., 3.96 mm O.D.) is centered in a larger tube (14.2 mm I.D., 19.0 mm O.D.) which is used to produce a small hydrogen pilot flame to stabilize the main ethylene flame. The experimental configuration was selected to closely follow that used by Turns and Myhr [17] for which a comparatively large data base with respect to radiation and NO_x emissions exists. The effect of the small amount of hydrogen ($\leq 1\%$ based on total mass flowrates) used for flame stabilization is expected to have minimal effect on the main flame structure [17]. The vertical burner is mounted on a translation device, which allows vertical and horizontal movements. Additionally, aluminum screens enclosing the burner region are installed to protect the flames from disturbances from the ambient air. A suction hood is positioned at the top to exhaust the combustion products. The suction rate was found not to affect the flame.

Ethylene, C_2H_4, was selected as the fuel since it is an intermediate species in the combustion of many higher molecular weight hydrocarbons, being formed by fuel fragmentation processes in the early flame stages [18]. In particular, this fuel has also been well characterized in previous in-house LII studies [12,13,19].
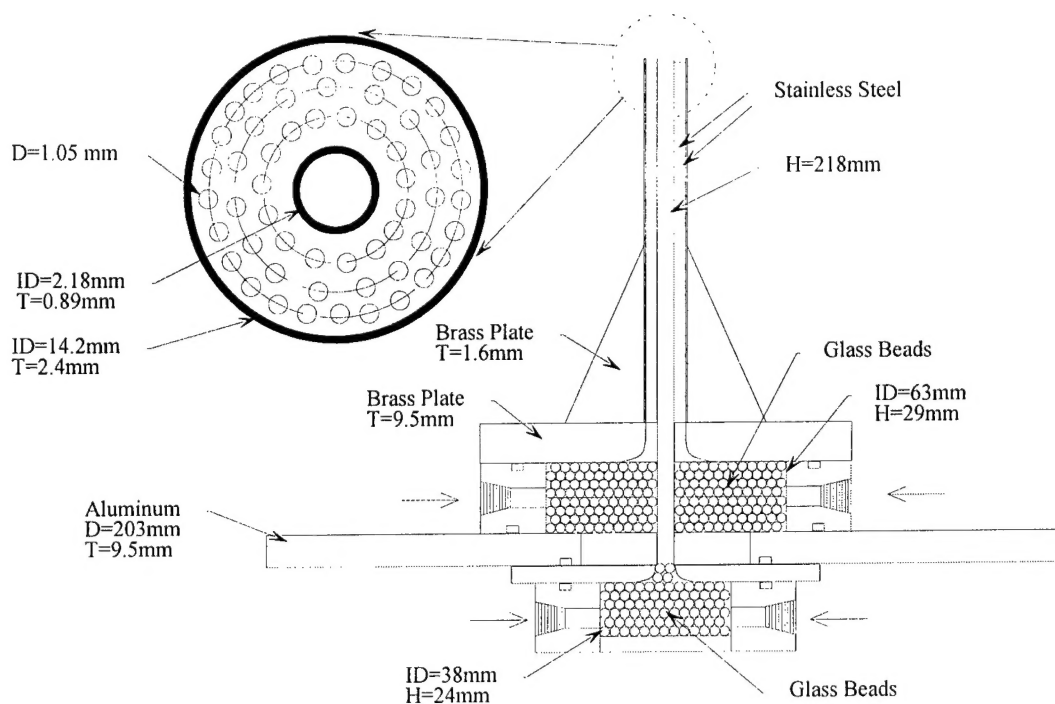

Fig. 1. Schematic of burner.

3

Experiments were conducted for various flames where the fuel jet Reynolds number, defined in terms of the fuel nozzle diameter and cold flow exit velocity, was varied. Specifically, for the 2.18 mm I.D. fuel nozzle, experiments were conducted for a Reynolds number range of 4000 to 23000.

Optical Setup

The optical configuration used for the two-dimensional LII and LIF measurements is schematically shown in Fig. 2. The intention in choosing this optical set-up was to keep the same spatial resolution for both measurements. For some experiments, joint measurements of soot volume fraction and OH· were made in order to observe their spatial relationships as the flow conditions were varied. For experiments where both measurements were not made simultaneously, the two different beam configurations were aligned to maintain the same system resolution and to avoid complications introduced by multiple optical arrangements.

The frequency-doubled beam at 532 nm of a Nd:YAG laser (Spectra-Physics GCR-270) was split into two beam propagation paths using a dichroic mirror (70% reflection and 30%
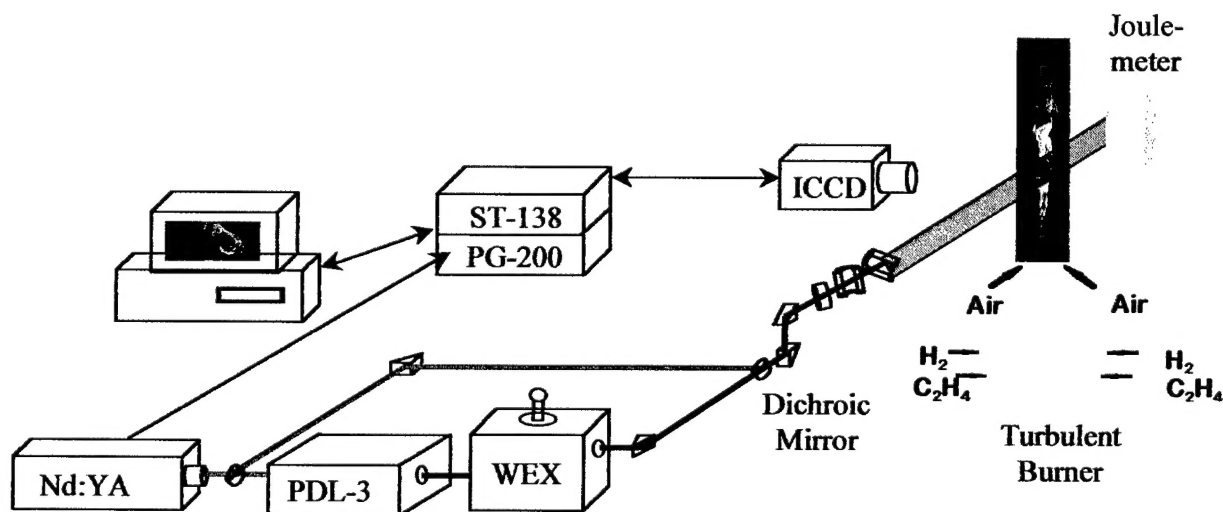

Fig. 2. Experimental set-up for 1-D or 2-D imaging of turbulent jet/air diffusion flames. OH· is excited by the laser wavelength of 283.55 nm corresponding to $Q_1(8)$ of the OH· band. Qualitative measurements of PAH are also obtained by de-tuning the laser off the OH· transition and observing the fluorescence signals. The interference filter and camera gate width for LII measurements are 400 ± 12.5 nm, $50 \sim 80$ ns initiated directly after the laser pulse, respectively. The OH· and PAH signals are collected from 300 nm to 380 nm with a 15 ns detection gate width. Simultaneous measurements of planar laser-induced incandescence (LII) of soot and laser-induced fluorescence (LIF) of OH· and PAH can also be carried out using one ICCD camera system.

transmission at 532 nm) in order to utilize the green (532 nm) beam for LII and the UV (283.55 nm) beam for OH-LIF measurements simultaneously. The reflected green beam is directed to pump the dye laser (Spectra-Physics PDL-3) circulating Rhodamine 590 dye (Exciton). The dye laser output is frequency-doubled using a commercial Wave Extender (Quanta-Ray WEX) to obtain the UV beam for the OH· excitation band of the $Q_1(8)$ transition. The $Q_1(8)$ line of the $A^2\Sigma$ -$X^2\Sigma(1,0)$ band of the 283.55 nm OH· transitions was selected in order to minimize the Boltzmann population correction with temperature, which was calculated to vary less than 5% over the range temperature 1400 - 2100K [20]. For the PAH measurement, LIF images of PAH were obtained by de-tuning the laser off the OH radical transition and observing the fluorescence signals.

The output of the WEX is then recombined with the 532 nm beam and both beams are passed through a combination of spherical and cylindrical lenses to produce a thin ($\sim 300\,\mu m$) planar laser sheet which passes through the center of the flame. The sheet beam intensity variation along the beam as it propagates across the flame was found to be less than 5% by measuring the Rayleigh scattering from air. The final spatial resolution is determined by either this beam width or the resolution of the ICCD detector as discussed below.

The signals are detected at an angle of 90° with respect to the light sheet using an intensified CCD camera (Princeton Instruments ICCD-576, 576×384 pixels). Since the flame width in the lower section of the flame height increases approximately linearly with distance from the nozzle tip, the field of view was set at about 83 mm horizontally and 53 mm vertically. The measured spatial resolution is approximately $280\,\mu m$ with a pixel grouping of 2×2 horizontally and vertically. A 288×3 pixel area was used for the line measurement of species quantities and generation of the probability distributions, which involved analysis of over 300 single-shot images. To improve the statistics, while preserving the spatial information, the probability distributions were determined by combining the neighboring 3×3 pixels to one position, as described by Dasch and Heffelfinger [9].

The quantitative LII measurements for soot concentration have been corrected for variations in the beam intensity using a beam profile determined from the light scattering measurements from air and for flame luminosity from a background subtraction procedure. The interference filter used in the LII measurement was 400 ± 12.5nm, and the gate-width was set at 50 ~ 80ns initiated directly after the laser pulse. The OH· and PAH signals were collected

in the range from 300 nm to 380 nm (WG305 and UG11 filters) with a 15 ns detection gate-width. PAH images were obtained by de-tuning the laser off the OH· transition and observing the fluorescence signals.

Calibration and Uncertainty

It is well established that the LII technique requires a careful calibration procedure; the soot volume fraction in a known sooting flame should be measured prior to the primary experiment [12]. As a consequence, a well-characterized ethylene laminar diffusion flame was selected as a calibration source, as in previous studies [12,13]. Soot volume fraction measurements were made in non-smoking ethylene-air diffusion flames with ethylene and air flow rates of 3.85 cm^3/s and 1060 cm^3/s, respectively. The soot volume fraction at the 10 mm ($f_v \sim 1.2$ ppm and $D_{63} \sim 65$nm; 1950.5 counts: 9.22 ppm, 248.3 counts: 1.18 ppm) height was selected as the calibration point. Since average peak soot volume fractions in turbulent ethylene flames are known to be below 2 ppm in moderately turbulent flames [5,7], this calibration location is considered to be most appropriate for the present studies.

The LII signal was carefully examined prior to conducting the primary test to determine the proper energy fluence level in the turbulent flame. First of all, the degree of symmetry of the averaged signal across the flame was tested at two different flame heights by varying the laser intensity. The two turbulent flame heights chosen included the region low in the flame in which soot is rarely observed and the region in the middle of the flame in which the highest average soot volume fraction is observed. For both heights, the symmetry of the signal across the flame was evaluated as a means to assure that the proper laser energy fluence had been selected. The final laser fluence that was sufficient to maintain the LII saturation regime was found to be approximately 0.5 - 0.7 J/cm^2 [12,14,19]. The laser energy transmitted through the flame was also monitored as shown in Fig. 2.

The uncertainty in measuring the LII signal involves the beam intensity variation as well as the sensitivity of the ICCD camera. To check the uncertainty associated with the LII signal, 200 single-shot measurements were made in the steady laminar diffusion flame. The signal fluctuations were found to be less than 10% at any given location. This uncertainty also includes uncertainties due to the laser intensity fluctuations and the efficiency of the optical system. The uncertainty associated with the average measurements was found to be less than 2%.

For the OH· and PAH measurements, the laser energy was monitored and maintained to minimize the energy variations using the lock-in system of the WEX.

Probability Density Function

The probability density function (pdf) can be described as $p(\psi) = \lim_{\Delta\psi \to 0} N_{\Delta\psi} / N_t \Delta\psi$, where $N_{\Delta\psi}$ is the number of sample points in the range of $\psi_1 \le \psi < \psi_1 + \Delta\psi$ and N_t is the total number of sample points for which an event occurs. In a turbulent flow, the distribution function encountered is sometimes continuous, and sometimes discontinuous. For example, in a soot volume fraction distribution there exists a significant degree of intermittency attributable to measurements corresponding to regions that contain no soot particles. Such measurements will be referred to as corresponding to the non-sooting mode statistics. When intermittency is considered, the pdf, $\wp(\psi)$, can be expressed as $\wp(\psi) = (1 - \Omega(\psi > 0)) \, \delta(\psi) + \Omega(\psi > 0) \, p(\psi)$, where $\delta(\psi)$ is a delta function at $\psi = 0$ and $\Omega(\psi > 0)$ refers to the intermittency index. The intermittency index is the fraction of the number of sample points in which $\psi > 0$. It is obvious that the lower the value of Ω, the higher the intermittency.

The example of the application of the pdf method presented below deals with the soot volume fraction, which is of most interest in the present study, but it can be also applied to any other turbulent property. The general structure of soot in turbulent flames consists of contributions from the sooting and non-sooting modes. Recalling that the non-sooting mode includes eddies without any soot concentrations, the pdf for the soot volume fraction can be described as $\wp(f_v) = (1 - \Omega(f_v > 0)) \, \delta(f_v) + \Omega(f_v > 0) \, N(f_v) / N_s \Delta f_v$ where N_s refers to the total number of sample points in a sooting mode and Δf_v denotes corresponding the soot volume fraction interval. $N(f_v)$ refers to the number of sample points that lie in the interval $f_{vl} \le f_v < f_{vl} + \Delta f_v$. The average soot volume fraction $\langle f_v^s \rangle$ in a sooting mode can be expressed as $\langle f_v^s \rangle = \sum n(f_v) f_v / N_s$. The ensemble-averaged soot volume fraction $\langle f_v \rangle$ can then be obtained as $\langle f_v \rangle = \Omega (f_v > 0) \langle f_v^s \rangle$. Thus, the-ensemble averaged soot volume fraction $\langle f_v \rangle$ is the product of the intermittency index and the average soot volume fraction $\langle f_v^s \rangle$ for conditions when soot is present, that is corresponding to sooting mode statistics. It is clearly evident that the average quantity is a strong function of the intermittency index.

7

3.0 RESULTS AND DISCUSSION

As discussed in the last section, the experiments were conducted using a fuel tube with a 2.18 mm I.D. For these experiments, the effects of changes in Reynolds number on the turbulent flame structure were studied. Obviously, for a fixed geometry, the Reynolds number was varied by changing the fuel injection velocity.

Images of Soot, OH· and PAH

The resulting two-dimensional images provide a wealth of information on the structure of the soot particle field in turbulent flames. Instantaneous soot volume fraction measurements indicated that the maximum observed soot volume fraction is nearly an order of magnitude higher than the temporally averaged mean value for the soot volume fraction [9,12]. This is due to the highly wrinkled structure of turbulent flames that leads to localized high concentrations of soot particles. When these results are temporally, and consequently spatially, averaged over the flame, the mean values are significantly lower. Since the impact of soot on combustion performance and emissions is dominated by local interactions, this information is key to understanding how soot affects combustion devices.

Instantaneous images of the soot, OH·, and PAH over the entire flame are illustrated in Fig. 3(a) for the Re = 12000 flame case. In the discussion of the results in this section, d is defined as the fuel tube diameter, whereas r and y are defined as the flame radial and axial locations, respectively. Each image section was collected at a different time and pieced together to give a composite representation of the flame. In this section, the focus is on the LII images of the soot particle field. The soot images indicate that the soot flowfield is highly intermittent and spatially isolated. This fact is not obvious in Fig. 3, but sequentially collected images do show high intermittency. It is apparent that the soot formation process does not occur as a spatially continuous process, as observed in laminar flames. A possible explanation for this observation is that at an early stage in the process of soot formation, which takes place near the fuel tube exit, the magnitude of the fluctuations of temperature [22] and velocity are relatively small. Transported by the momentum fluctuations due to velocity fluctuations, this initial soot material is carried to an axial position where the temperature fluctuation range begins to increase. At this point, during the transport of this newly-formed soot material, the soot chemical formation mechanism occurs under a variety of temperature and velocity conditions, since soot chemical reaction time is known to be on the order of a few milliseconds [9]. Soot is most rapidly formed

when the temperature lies between 1200 and 1800K [7]. High concentrations of soot particles will form in higher temperature regions having a small temperature fluctuation range, while the low concentrations of soot are formed in regions exhibiting a broad temperature fluctuation range [6]. Therefore, two parameters determine the soot field structure: the velocity effect on the spatial distribution pattern and the temperature effect on the chemical formation process.

OH· is often considered an ideal intermediate species for flame structure studies, as well as a good marker of the flame front for some flow conditions [23]. Moreover, OH· is abundant and yields a high signal-to-noise ratio in terms of fluorescence measurements compared to other species. This fact enables direct measurement of OH·, yielding qualitative information regarding information about the reaction zone associated with a specific flow condition.

An instantaneous image of OH· also is shown in Fig. 3(a). The structure of the OH· region broadens and becomes highly wrinkled and spatially distributed as the axial position in the flame increases. As expected, OH· regions become more convoluted with increasing downstream distance. Specifically, OH· at the beginning of the fuel injection process occurs in
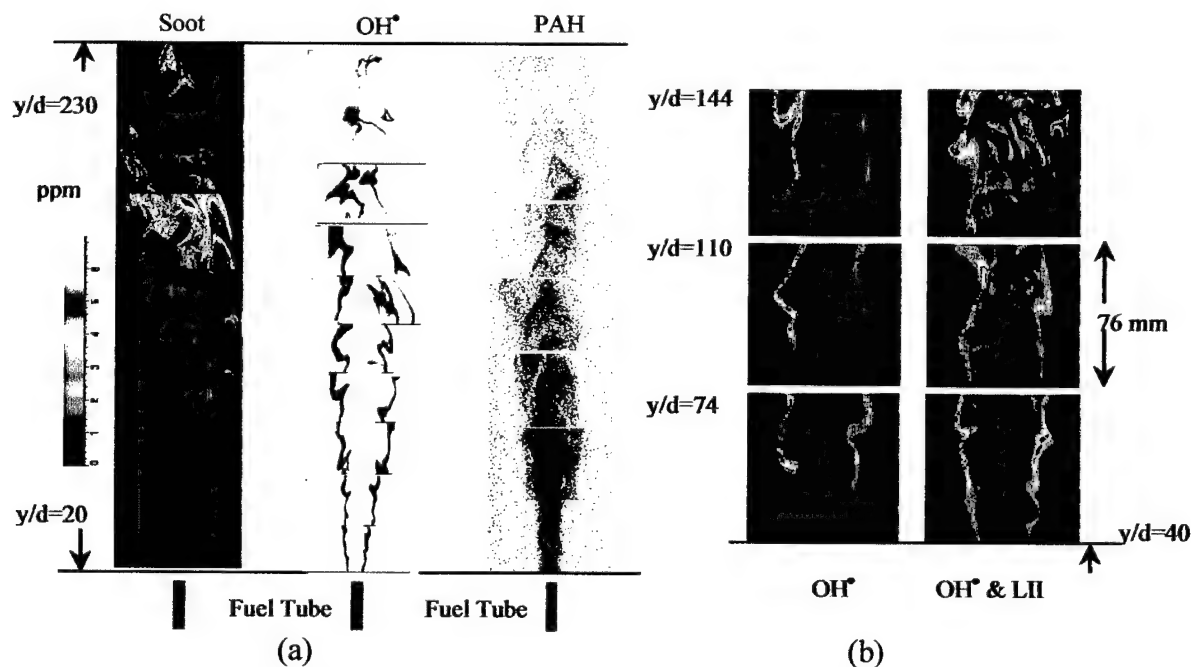

Fig. 3. General structure of soot, OH· and PAH fields (a) and joint measurements of soot and OH· (b) at Re=12000 (2.18 mm I.D. fuel tube burner). For (a), each image section is collected at a different time and pieced together to give a composite representation of the flame. For the joint measurements of soot and OH· in (b), a OH· band filter was used for both signals with a wide gate width of ~80 ns. The large signal ratio between LIF to LII measurements was used to discriminate between the two signals since both signals are captured on the same ICCD.

9

thin regions that increase in thickness with downstream distance. These thickness variations regarding the flame conditions and positions will be examined later. Because of slow three-body recombination reactions, OH· typically exhibits super-equilibrium concentrations and is observed to persist at lower concentrations even away from the flame zone. Note that the OH· image indicates a continuous zone along the flame axis, which is distinctly different from the soot structure shown in Fig. 3(a).

In contrast to those two images, the instantaneous PAH image represented on a log-scale shows that PAH is formed along the jet axis and spreads out radially with increasing axial position. Furthermore, above the middle of the flame, the signal is significantly weaker compared to the background noise.

The joint images of OH· and LII soot signals are shown in Fig. 3(b). When the green and UV beams are focused simultaneously into the flame, as shown in Fig. 2, the LII and OH-LIF signals can be observed simultaneously when recorded on the same camera if they are spatially distinct. Increasing the camera gate-width sufficiently to capture the two signals can compensate for the difference in propagation times for the two laser beams to reach the flame. In this case, the filter used previously to isolate of the OH· bands was used for both signals. The gate-width for simultaneous measurement was set at ~80 ns. Because two images were collected on a single camera, care was taken to ensure that the UV energy resided within a linear fluorescence regime and the large signal ratio between the LIF to LII measurements was used to differentiate between the two signals. Before simultaneous measurements were performed, more than 50 single-shot images were collected and checked carefully to ensure two distinct images were clearly observed. Thus, the resulting images are used only for qualitative analysis. Quantitative analysis would require a two-camera system to evaluate the two signals.

For axial locations below approximately half the flame height, the OH· region is not broadly distributed and likely correlates with the flame zone. Higher in the flame, highly distributed and wrinkled OH· zones are usually observed, which makes it very difficult to differentiate between the LII and OH· since both signals were collected on one camera. The flow field patterns in the OH· and LII images are clearly different in that the soot field is isolated inside the OH· zone at lower axial locations. The few observations of overlapped signals of OH· and LII were seen at lower flame heights, which confirms results observed in previous research [24].

In summary, the images of soot, OH·, and PAH indicate that three distinct zones associated with soot formation/destruction regions exist. The first region is characterized by rapid soot growth in which the soot particles and OH radicals exist in distinctly separate regions of the flame. As the Reynolds number is increased by increasing the fuel injection velocity (images not shown here), the soot particle-laden region shifts towards the center of the flame. Following this region of growth, which is demarcated clearly by the absence of PAH fluorescence, as indicated from the LIF-PAH imaging measurements, a mixing-dominated zone is observed that is strongly affected by increases in the Reynolds number (increasing velocity). Mixing processes in this region affect the maximum soot volume fraction measured in an individual flame with the soot volume fraction decreasing with increasing Reynolds number (increasing velocity). The final region is characterized by an overlapping of the soot particle and OH radical fields that leads to oxidation of the soot particles. Only the high concentration regions formed lower in the flame survive this region to be emitted from the flame as smoke.

Soot Volume Fraction Profiles

The effect of turbulence on the average soot generation along the flame centerline is examined in Fig. 4. The range of root-mean-square (rms) values (fluctuations) also is plotted in the bottom of the figure. The results show that at a given axial location, the soot concentration decreases as the Reynolds number is increased by increasing the fuel velocity. The initial soot formation is delayed spatially and occurs further downstream, while the soot oxidation takes place slightly earlier in the streamwise direction. The higher velocity (i.e., higher Reynolds number flames) delays the initial inception of soot formation because of the shorter residence time available for soot particles to form. The soot particle residence time is approximately inversely related to the Reynolds number at a given axial location [25].

The axial location where the maximum $\langle f_v \rangle$ occurs is relatively insensitive to the Reynolds number and corresponds to approximately half the flame height. As pointed out by Kent and Bastin [4], the axial location of the maximum $\langle f_v \rangle$ is independent of the flow conditions with the same fuel, while this location changes depending on the fuel type. The soot formation region is classified as the zone below the axial position where the maximum $\langle f_v \rangle$ occurs, whereas the soot oxidation region refers to the zone above the location at which the maximum $\langle f_v \rangle$ occurs ($\sim y/d = 150$).
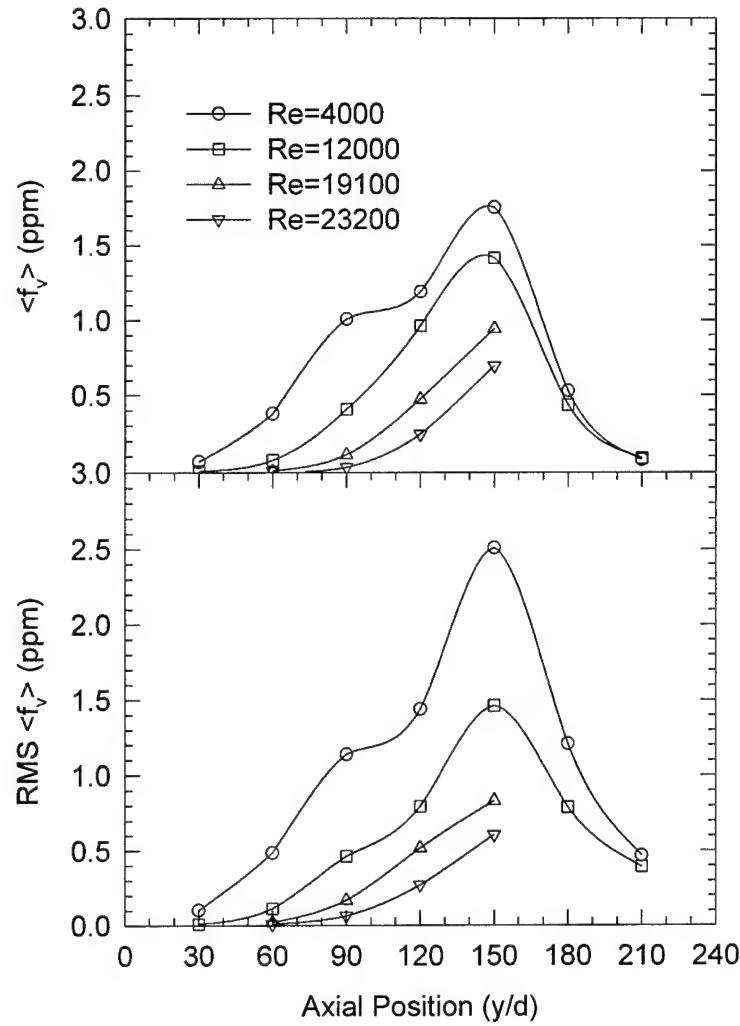
Fig. 4. Axial profiles of average (top) and RMS (bottom) soot volume fractions $\langle f_v \rangle$ on the jet axis for four Reynolds number flames (2.18 mm I.D. fuel tube burner).

Radial profiles of average soot volume fractions for three Reynolds number flames are presented in Fig. 5. For a given Reynolds number, the average soot volume fraction radial profiles differ at various axial locations. For axial locations below approximately half the flame height the average soot volume fraction increases with increasing radial distance to a maximum value and then decreases. In contrast, at axial distances greater than half the flame height, the average soot volume fraction is highest along the centerline and decreases with radial distance. Momentum carries soot to the jet axis upstream, while buoyancy drags soot off the jet axis further downstream. The primary effect of the turbulence is to broaden the radial soot

concentration profiles at a given axial position [7]. For example, the soot concentration at
y/d = 90 for the Reynolds number of 8000 has a relatively narrow double-humped profile, but the
profile becomes broader with increasing Reynolds number. For all cases shown, maximum soot
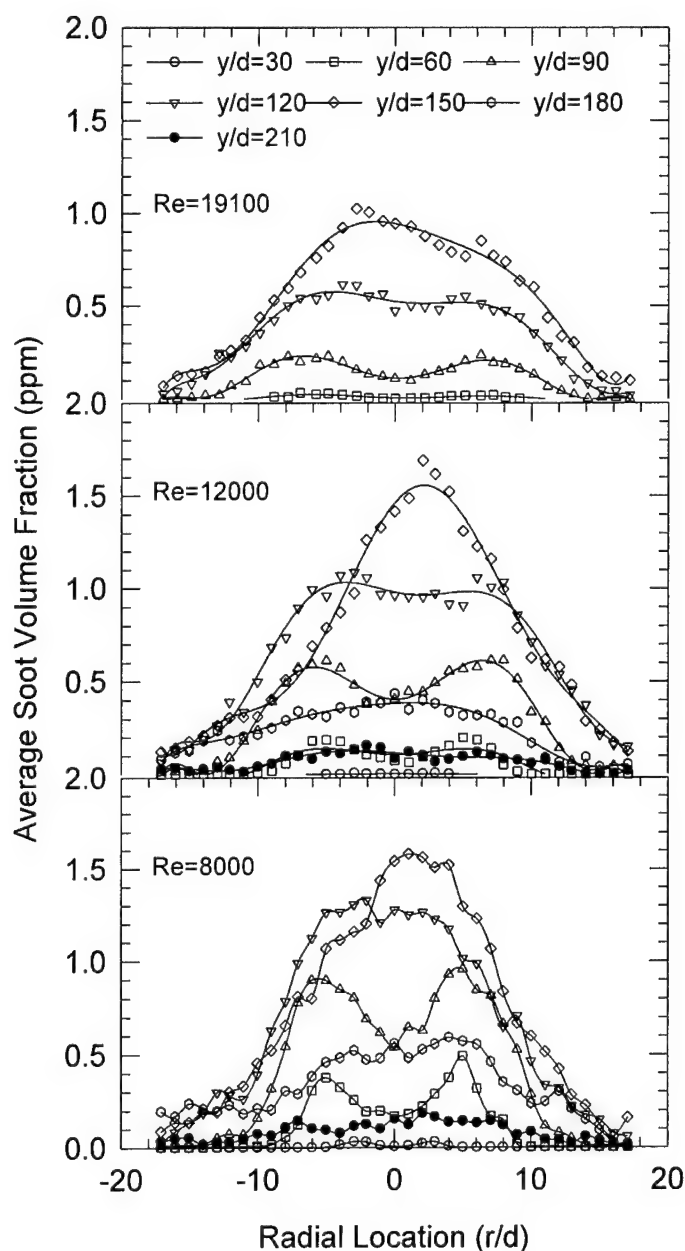volume fractions are observed to be less than 2 ppm. Note that the RMS soot volume fraction

Fig. 5. Radial profiles of average soot volume fraction $\langle f_v \rangle$ for the three Reynolds number flames
(2.18 mm I.D. fuel tube burner). The peak soot volume fraction is less than 2 ppm (particles per
million) for all cases. The soot radial profiles broaden with increased Reynolds number
(increased velocity) at a given axial positions.

fluctuations can be as large as the average soot volume fraction near the jet axis. For the flames with Reynolds numbers of 4000 and 8000, RMS soot volume fraction values achieve magnitudes as large as 8 times the average soot volume fraction close to the flame boundary, mainly due to flame movement (flapping) as well as air entrainment [9].

Integration of the Soot Volume Fraction Profiles

Total soot production at a given axial position can be obtained by integrating the radial profiles of the soot volume fraction over the radial coordinate, expressed by $\sum < f_v > = \pi \left(\int_- < f_v > r dr + \int_+ < f_v > r dr \right)$. The integration has been carried out over both the positive (+r/d) and negative (-r/d) directions from the flame centerline since the observed flames are asymmetric [22]. Some errors associated with the integration due to the physical limits of the field of view of the camera detector exist, and they depend on the Reynolds number and axial location. For example, the flame occasionally fluctuates radially and thus sometimes extends beyond the image frame, particularly above the middle of the flame. The frequency at which the signal extends beyond the image frame increases as the axial location approaches the flame tip, mainly due to buoyancy effects. This effect becomes more pronounced as the Reynolds number of the flame increases. Consequently, the integration has been conducted for flames for which the Reynolds number ranges from 4000 to 12000, and the results do not completely treat all features of the flames studied, but, rather reflect the general trend.

No significant variations in the total soot concentration as function of Reynolds number (increased velocity) were observed except for Re = 4000. This lack of variation is due to the fact that the flame widths are nearly the same for each case and radial profiles of average soot concentration are similar regardless of the Reynolds number in these intermediate Reynolds number flames [4]. Although the primary effect of turbulence is to broaden the radial soot concentration profile, as observed in Fig. 5, at the same time the overall amount of soot particles is decreasing at a given axial position. These two effects result in comparable integrated soot concentrations regardless of the Reynolds number, as shown in Fig. 6. It is also evident that the integrated soot volume fractions have a self-similar profile. A similar observation is also true for the radial profiles of soot concentration for all Reynolds numbers studied.
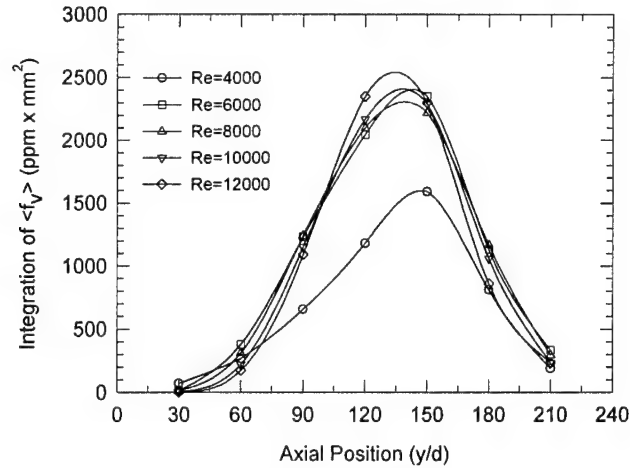
Fig. 6. Axial profiles of integrated soot volume fraction $\sum <f_v>$ as obtained from $\sum <f_v> = \pi\left(\int_+ <f_v> rdr + \int_- <f_v> rdr\right)$ for both positive (+r/d) and negative (-r/d) directions from the flame centerline.

Soot Volume Fraction and OH· Zone Thickness

From the OH· images shown in Fig. 3, most have two continuous regions on both sides, -r/d and r/d upstream, whereas they have one continuously distributed zone well downstream in the axial direction. The spatial structure of OH· has been well-characterized in terms of the thickness, orientation, distribution, etc., in hydrogen and hydrocarbon flames by Seitzman et al. [26], Johnson et al. [27], and Chen and Goss [28]. In contrast, soot images observed in the present studies have many isolated zones, which leads to difficulty in determining the zone thickness. In terms of average soot volume fraction, the maximum signal intensities in each of the individual images are important for characterizing the soot formation process. For this reason, the zone thickness at a particular axial position was measured by counting the number of pixels along a line image crossing the region of interest for each species (f_v or OH·) representing the full width at half maximum intensity (FWHM) at the location of the maximum signal intensity in each of the images obtained. Since the laser beam is perpendicular to the flame axis, there is a potential error in the zone thickness measurements due to orientation effects between the flame and the laser beam. Following Ref. 27, the actual zone thickness is obtained from the shortest line across the structure zone.

The axial dependence of the soot and OH· zone thickness is presented in Fig. 7 for five Reynolds number flames (2.18 mm I.D. fuel tube burner). The thicknesses of the soot and OH·

15

zones are significantly different in terms of their size. The soot zone thickness increases nearly linearly from a value of 0.5 mm to 2.5 mm in the soot formation region (y/d ≤ 150) and decreases to 1 mm further downstream at a y/d of 210. The axial variation of the soot zone thickness is almost identical for the range of Reynolds numbers studied here. In contrast, the OH· zone thickness changes little in the soot formation region regardless of the Reynolds nuumber, but it begins to change dramatically in the soot oxidation region (y/d ≥ 150). This effect is particularly pronounced at y/d = 180. The OH· zone thickness is observed to increase by nearly a factor of two near y/d = 180 as the Reynolds number increases from 4000 to 12000 as the jet velocity increases.
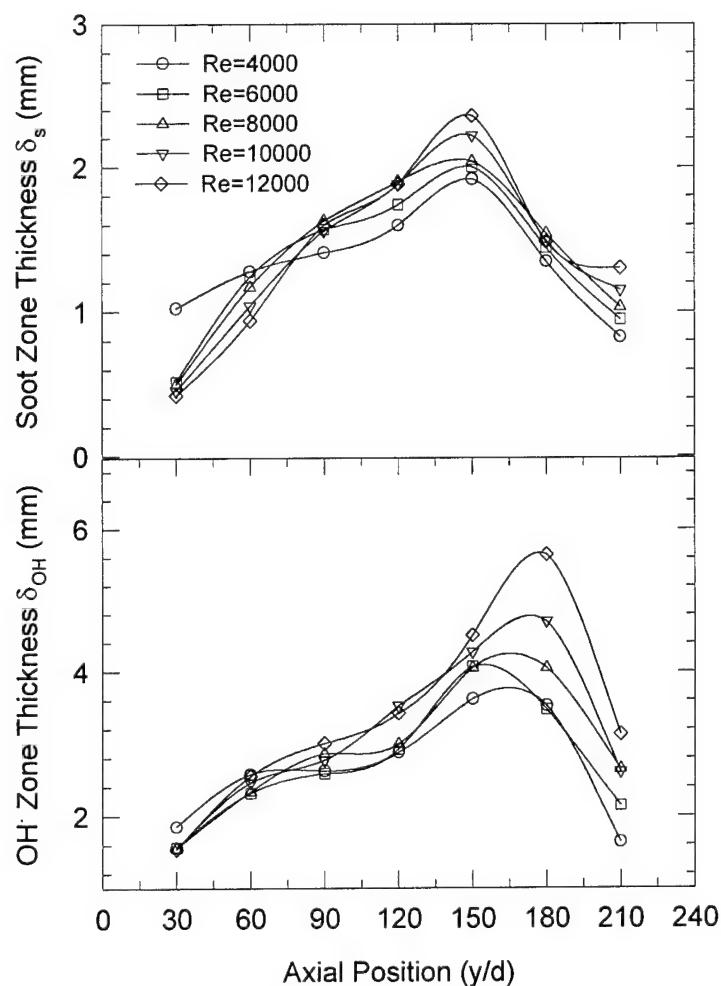

Fig. 7. Axial profiles of the soot (top) and OH· (bottom) zone thickness. The zone thickness at a particular axial position is measured by counting the number of pixels along a line image crossing the region of interest for each instantaneous signal representing the full width at half-maximum intensity (FWHM) at the location of the maximum signal intensity in each of individual images obtained.

16

The axial locations at which the maximum zone thickness for OH· and soot occurs are spatially different from each other. Specifically, the peak soot zone thickness occurs around $y/d = 150$, whereas the peak OH· zone thickness is observed close to $y/d = 180$ for all the Reynolds number cases. Hence, the spatial distribution of the OH· zone plays a major role in reducing soot in terms of its absolute magnitude and soot zone thickness. The evolution of the spatial distribution of the OH· zone in the flame eventually determines where soot growth ceases and subsequently leads to reductions in the amount of soot particles in the soot oxidation region.

Intermittency and High Soot Volume Fraction Regions

One of the most noteworthy features of the LII images is the occurrence of a few eddies containing high soot concentration in the oxidation zone of the flame ($y/d \approx 210$). In order to investigate soot concentrations within these soot-containing eddies (sooting mode), the soot volume fractions corresponding to the sooting mode $\langle f_v^s \rangle$ are calculated as $\langle f_v^s \rangle = \langle f_v \rangle / \Omega(f_v > 0)$. Fig. 8 shows the intermittency index (top) and $\langle f_v^s \rangle$ (bottom) for the Re = 12000 flame (2.18 mm I.D. fuel tube burner). The lower values of the intermittency index Ω indicate higher intermittency.

From the results shown in Fig. 8 several observations can be made. First, the radial profile of Ω is a strong function of axial location and increases until the position $y/d=120$, which is just below the location of the maximum soot volume fraction near $y/d = 150$. Downstream of this location, air entrainment into the soot oxidation region reduces the soot volume fraction and soot zone thickness, as discussed previously, which is reflected in both the intermittency index and $\langle f_v^s \rangle$. At all locations shown in Fig. 8 with the exception of $y/d = 30$, the radial profiles of $\langle f_v^s \rangle$ are comparable. In particular, high soot concentrations with high intermittancy are observed even close to the flame tip ($y/d = 210$). Comparisons with the average soot volume fraction, as shown in Fig. 5, indicate much wider variations in the soot concentration with axial position. This wider variation is directly a result of the effect of intermittency. Dasch and Heffelfinger [9] pointed out a similar observation from their light scattering studies of turbulent ethylene flames and noted that a large amount of soot is observed in the higher intermittency region, while the soot concentration is low in the lower intermittency region.
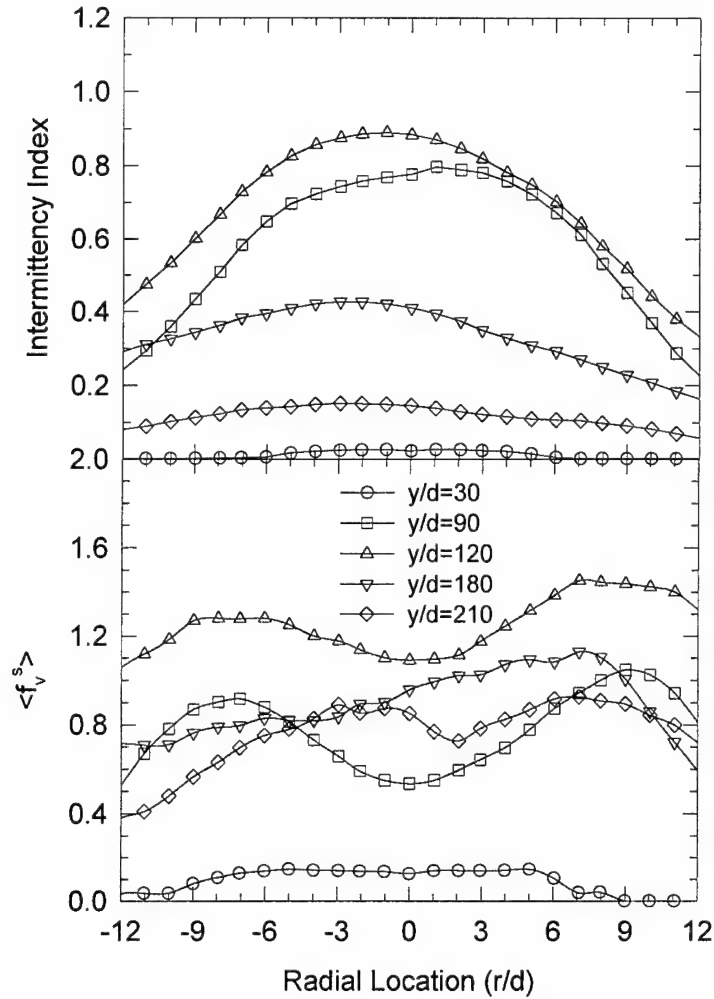
Fig. 8. Intermittency index (top) and soot volume fractions corresponding to the sooting mode (bottom) for Re=12000 flames (2.18 mm I.D. fuel tube burner) as a function of axial position.

Probability Density Functions

Probability density functions (pdf) for soot volume fractions are plotted in Fig. 9. In the top half of the figure, soot volume fraction pdfs at various radial locations for the y/d=120 axial location in the Re = 12000 flame are shown. In the bottom half of the figure, the soot volume fraction pdfs for various Reynolds number are shown for the centerline position at y/d = 120. The radial profiles of the pdfs plotted in the top figure show the distribution of the instantaneous values of soot volume fractions. These radial profiles can be compared to the average soot concentration profile plotted in Fig. 5 for y/d = 120 axial position, which exhibits a flat region around the flame centerline, and then rapidly decreases with increased radial location.
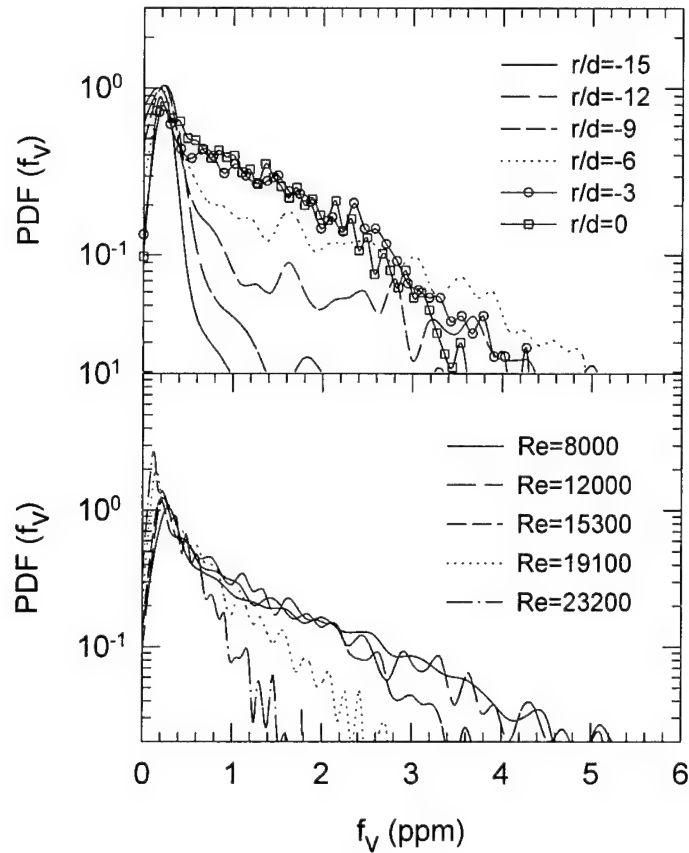
18

Fig. 9. Probability density functions for soot volume fractions as a function of radial location at y/d=120 for the Reynolds number of 12000 flames (top) and as a function of Reynolds number on the jet axis (bottom) taken at r/d=0 and y/d=120. Results are for the 2.18-mm I.D. fuel tube burner.

At this axial location, the intermittency is very low ($\Omega > 0.5$), as shown in Fig. 8 (top). Meanwhile soot concentrations in the sooting mode, $\left\langle f_v^s \right\rangle$, further from the flame centerline (see Fig. 8, bottom, for example) exhibit a relatively flat behavior as a function of radial position for y/d = 120. The instantaneous soot volume fraction away from the flame axis (for example, r/d = −15) is observed to be no higher than ~ 1 ppm, compared to ~ 5 ppm at the flame axis. Thus, air entrainment, which controls both local mixing and intermittency, profoundly affects the soot formation processes. The regions having low soot concentrations are oxidized rapidly, while the regions with large soot concentrations are affected less (see the soot pdf at r/d = -9). Thus, soot emissions observed higher in the flame are a result of the survival of these large soot concentration regions.
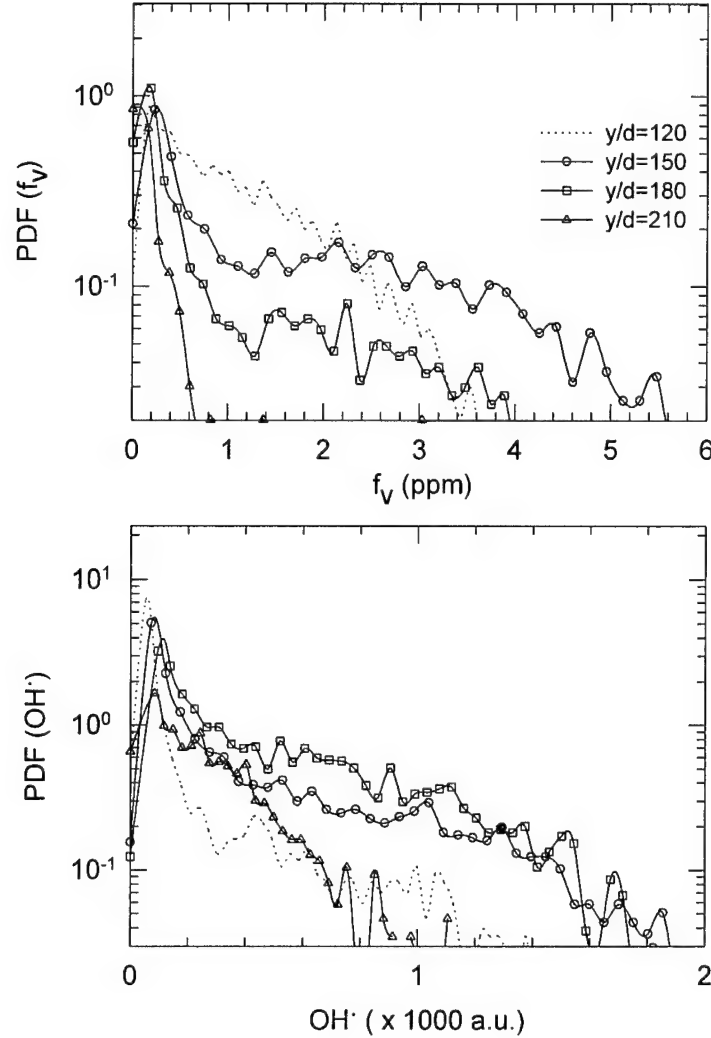
Fig. 10. Probability density functions for soot volume fractions (top) and OH· (bottom) taken at r/d=0 in the Reynolds number of 12000 flames (2.18 mm I.D. fuel tube burner).

The effect of different mixing rates, as represented by the Reynolds number (jet velocity) variations, indicates that regions of higher concentrations of soot particles disappear with increasing Reynolds number, implying that the average soot volume fraction decreases. For all cases examined, the pdf shapes are greatly skewed, and they have nearly exponential distributions. Such observations can be clearly seen from the pdfs on the centerline, where the pdfs having higher soot volume fractions do not decrease as rapidly as those pdfs with lower soot volume fractions. For example, the pdfs for the Reynolds number flames of 8000, 12000, and 15300 do not decrease as quickly as the pdfs for the higher Reynolds number flames of 19100 and 23200. This effect is also attributable to both increased mixing and, to some degree, to the shorter residence time for high Reynolds number flames, which limits the time for soot particle

20

formation in the flame. In other words, the turbulence effect on the soot formation is more pronounced in the higher Reynolds number flames due to both mixing and residence time effects.

Pdfs of soot and OH· concentrations on the jet axis for the Re=12000 flame are shown in Fig. 10. First of all, the soot pdfs show that there is relatively little soot observed up to $y/d = 60$. Also, OH· is not observed up to $y/d = 90$. Soot concentration slowly increases up to $y/d = 150$. At the same time, OH· concentration rapidly increases in terms of the slope of the pdf distribution. The axial position of highest soot concentration is also the position of highest OH· concentration. Further downstream, at $y/d \geq 180$, the OH· concentration is still significant, but the soot decreases quickly. Soot pdfs observed for the axial positions of $y/d = 150$ and $y/d = 180$ show that soot particles in high soot concentration regions are more slowly oxidized than those in low soot concentration regions as noted above. Close to the flame tip location, most of the soot particles are oxidized while relatively large concentrations of OH· are apparent. A strong spatial correlation was found between soot and OH· such that OH· plays a significant role in oxidizing soot particles, which also was observed in laminar diffusion flame studies [16].

4.0 SUMMARY

Turbulent ethylene/air jet diffusion flames over a Reynolds number range from 4000 to 23000 were experimentally investigated to enhance the understanding of the soot formation processes. Particularly, the recently established laser-induced incandescence technique was used to not only visualize the turbulent soot field, but also to provide new quantitative measurements of the soot particle field under turbulant flame conditions. Soot formation/oxidation mechanisms have been studied under various flame conditions and results are summarized below.

The soot field images indicate that the soot formed consists of highly intermittent, anisotropic, thin regions oriented along the flame direction, and isolated in the turbulent diffusion flame. In contrast, the OH· field exhibits spatially wrinkled and distributed features introduced by turbulence. Soot characteristics are influenced by the effect of velocity on the spatial distribution of the soot particle field and the effect of temperature on the chemical soot formation process. In contrast to the OH· and soot particle fields, the PAH field is observed to lie very close to the fuel nozzle exit and disappears quickly with increasing mixing rate.

Imaging results for PAH, soot particles, and OH· indicate three distinct soot formation/oxidation related regions. In the soot growth region, the OH· and soot particle fields lie in distinctly different locations, whereas the OH· is located further from the flame centerline. Laser-induced fluorescence imaging of PAH clearly demarcates the soot growth region in these flames. Following this region of rapid soot particle growth, a mixing-dominated zone is observed that is strongly affected by increases in the Reynolds number. The final region involves the interaction of the OH· and soot particle fields. Here, the OH· and soot regions overlap, leading to rapid oxidation. Only the high soot concentration regions formed lower in the flame survive this process, to be emitted from the flame as smoke.

Turbulence has an influence on the amount of soot produced in the flame but does not tend to affect the characteristic soot profiles, since the higher mixing rate delays the initial inception of soot formation due to the short residence time of soot. The primary effect of turbulence is to broaden the radial soot concentration profiles at a given axial position. Profiles of radial soot concentrations and integrated soot concentrations have self-similarity for intermediate flame regimes at given axial positions, while the amount of soot is reduced with increasing Reynolds number. For all the flames investigated, the maximum soot volume fractions are observed to be less than 2 ppm.

The soot zone thickness varies linearly from 0.5 mm to 2.5 mm in the formation region, and then decreases to 1 mm further downstream regardless of the mixing rate. However, a variation almost twice as large in the thickness of the OH· zone as compared to the soot zone thickness is observed. In addition, the pdf of soot soot volume fraction at a given location displays an exponential distribution, similar to observations using laser light scattering measurements provided by Dasch and Heffelfinger [9]. The intermittency index for soot is strongly a function of the flame height such that the intermittency index increases until the occurrence of maximum soot volume fraction.

Based on the average soot volume fraction, soot and OH· zone thicknesses, and the pdfs for OH· concentration and soot volume fraction, a detailed understanding of the interrelationships between OH· and soot formation/destruction processes was determined for these flames. Below the region where the soot volume fraction achieves a maximum (~ y/d=150), the OH· and soot particle fields are distinct and separated spatially. In this region, both soot and OH· increase in concentration as well as in spatial extent. Distinct differences were observed for the soot formation region, which occurs lower in the flame, as the Reynolds number (jet velocity) was varied. These differences are argued to be related to residence time and mixing effects. Near and above the location where the soot volume fraction achieves its maximum, the OH· and soot particle fields overlap spatially. The resulting soot oxidation process causes the soot volume fraction to decrease rapidly. For the oxidation region, the behavior of the soot particle and OH· fields in terms of their zone thickness were observed to be similar as the Reynolds number varied.

5.0 REFERENCES

[1] Magnussen, B.F., *Fifteenth Symposium (International) on Combustion*, The Combustion Institute, Pittsburgh, 1974, p. 1415.

[2] Magnussen, B.F., Hjertager, B.H., Olsen, J.G. and Bhaduri, D., *Seventeenth Symposium (International) on Combustion*, The Combustion Institute, Pittsburgh, 1978, p. 1383.

[3] Kent, J.H. and Honnery, D., *Combust. Sci. and Technol.* 54:383 – 397 (1987).

[4] Kent, J.H. and Bastin, S.B., *Combust. Flame* 56:29 - 42 (1984).

[5] Sivathanu, Y.R. and Faeth, G.M., *Combust. Flame* 81:133 – 149 (1990).

[6] Sivathanu, Y.R. and Faeth, G.M., *Combust. Flame* 81:150 – 165 (1990).

[7] Coppalle, A. and Joyeux, D., *Combust. Flame* 96:275 – 285 (1994).

[8] Turns, S.R., Lovett, J.A. and Sommer III, H.J., *Combust. Flame* 77: 405 – 409 (1989).

[9] Dasch, C.J. and Heffelfinger, D.M., *Combust. Flame* 85:389 – 402 (1991).

[10] Melton, L.A., *Applied Optics* 23:2201 - 2208 (1984).

[11] Hofeldt D.L., *SAE Technical Paper 930075*:33 - 45 (1993).

[12] Quay, B., Lee, T.-W., Ni. T. and Santoro, R.J., *Combust. Flame* 97:384 – 392 (1994).

[13] Gupta, S.B., Ph.D. dissertation, Department of Mechanical Engineering, The Pennsylvania State University, 1996.

[14] Shaddix, C.R. and Smyth, K.C., *Combust. Flame* 107:418 – 452 (1996).

[15] Geitlinger, H., Streibel, TH., Suntz, R. and Bockhorn, H., *Twenty-Seventh Symposium (International) on Combustion*, The Combustion Institute, Pittsburgh, 1998, p. 1383.

[16] Puri, R., Moser, M., Santoro, R.J. and Smyth, K.C., *Twenty-Fourth Symposium (International) on Combustion*, The Combustion Institute, Pittsburgh, 1992, p.1015.

[17] Turns, S.R. and Myhr, F.H., *Combust. Flame* 87:319 - 335 (1991).

[18] Westbrook, C.K., Dryer, F.L. and Schug, K.P., *Nineteenth Symposium (International) on Combustion*, The Combustion Institute, Pittsburgh, 1998 p. 153.

[19] Ni. T., Pinson, J.A., Gupta, S.B. and Santoro, R.J., *Applied Optics* 34: 7083 – 7091 (1995).

[20] Dieke, G.H. and Crosswhite, H.M., *J. Quant. Spectrosc. Radiat. Transfer*, 2:97 - 199 (1962).

[21] Lee, S.-Y. and Santoro, R.J., *Fall Technical Meeting, The Eastern States Section of the Combustion Institute*, 1997.

[22] Lee, S.-Y., Ph.D. dissertation, Department of Mechanical Engineering, The Pennsylvania State University, 1998.

[23] Norton, T.S. and Smyth, K.C., *Combust. Sci. and Technol.* 76:1 - 20 (1991).

[24] Gupta, S.B., Ni, T. and Santoro, R.J., *Fall Technical Meeting, The Eastern States Section of the Combustion Institute*, 1994.

[25] Tieszen, S.R., Stamps, D.W. and O'hern, T.J., *Combust. Flame* 106:442 – 466 (1996).

[26] Seitzman, J.M., Ungut, A., Paul, P.H. and Hanson, R.K., *Twenty-Third Symposium (International) on Combustion*, The Combustion Institute, Pittsburgh, 1990 p. 637.

[27] Johnson, A.W., Sreenivasan, K.R. and Winter, M., *Combust. Sci. and Technol.* 89:1 – 7 (1993).

[28] Chen, T.H. and Goss, L.P., *Combust. Sci. and Technol.* 79:311 – 324(1991).

6.0 PUBLICATIONS/THESES

1. Lee, S.-Y., <u>Detailed Studies of Spatial Soot Formation Processes in Turbulent Ethylene Jet Flames</u>, Ph.D. Dissertation, The Pennsylvania State University, 1998.

2. Lee, S.-Y. and Santoro, R., "Observation of Integral Length Scales of Soot Particles, OH Radicals and PAH in Turbulent Diffusion Flames," *First Joint Meeting of the U.S. Sections of the Combustion Institute: Western States, Central States, Eastern States, 1999.*

3. Lee, S.-Y. and Santoro, R., "Statistical Determination of Fuel Regimes and Its Implication Using CARS System in Turbulent Ethylene Jet Flames," *The Tenth Annual Symposium, Propulsion Engineering Research Center, NASA Marshall Space Flight Center, 1998.*

4. Lee, S.-Y., Pal, S., and Santoro, R., "Temperature and Unmixed Fuel Measurements in Turbulent Jet Flames by Using Coherent Anti-Stokes Raman Spectroscopy," *Fall Technical Meeting, The Eastern States Section of the Combustion Institute, 1997.*

5. Lee, S.-Y. and Santoro, R., "Imaging Studies of Soot Formation in Turbulent Ethylene Jet Flames," *Fall Technical Meeting, The Eastern States Section of the Combustion Institute, 1997.*

7.0 PARTICIPATING PROFESSIONALS

Prof. Robert J. Santoro, Professor of Mechanical Engineering, Principal Investigator

Dr. Seong-Young Lee, Graduate Research Assistant and Research Associate

Mr. Larry Horner, Technician

8.0 PRESENTATIONS

1. "Soot Formation Studies in Laminar and Turbulent Diffusion Flames," Santoro, R. J, invited seminar presented at the Department of Mechanical and Aerospace Engineering Seminar Series, Princeton University, December 9, 1997, Princeton, NJ.

2. "Applications of Laser-Based Diagnostics to High Pressure Rocket and Gas Turbine Combustor Studies," Santoro, R. J., presented at the 20th AIAA Advanced Measurement and Ground testing Technology Conference, June 15-18, 1998, Albuquerque, NM.

3. "Non-Intrusive Diagnostics in High Pressure Combustion Environments," Santoro, R. J. invited presentation presented at 1999 National Heat Transfer Conference, August 15-17, 1999, Albuquerque, NM.

4. "Soot Formation Processes in Turbulent Ethylene/Air Diffusion Flames," Santoro, R. J, invited seminar presented at the Department of Mechanical Engineering, University of Delaware, Oct. 1, 1999, Newark, NJ.

9.0 HONORS

Appointed Distinguished Professor of Mechanical Engineering, The Pennsylvania State University, January 2000.

Awarded the 2000 Penn State Engineering Society Premier Research Award, February 2000.